ADVANCED MATERIALS
www.advmat.de

Berry Curvature Dipole Induced Giant Mid-Infrared Second-Harmonic Generation in 2D Weyl Semiconductor

Qundong Fu, Xin Cong, Xiaodong Xu, Song Zhu, Xiaoxu Zhao, Sheng Liu, Bingqing Yao, Manzhang Xu, Ya Deng, Chao Zhu, Xiaowei Wang, Lixing Kang, Qingsheng Zeng, Miao-Ling Lin, Xingli Wang, Bijun Tang, Jianqun Yang, Zhili Dong, Fucai Liu, Qihua Xiong, Jiadong Zhou, Qijie Wang, Xingji Li,* Ping-Heng Tan,* Beng Kang Tay, and Zheng Liu**

Due to its inversion-broken triple helix structure and the nature of Weyl semiconductor, 2D Tellurene (2D Te) is promising to possess a strong nonlinear optical response in the infrared region, which is rarely reported in 2D materials. Here, a giant nonlinear infrared response induced by large Berry curvature dipole (BCD) is demonstrated in the Weyl semiconductor 2D Te. Ultrahigh second-harmonic generation response is acquired from 2D Te with a large second-order nonlinear optical susceptibility ($\chi^{(2)}$), which is up to 23.3 times higher than that of monolayer MoS_2 in the range of 700–1500 nm. Notably, distinct from other 2D nonlinear semiconductors, $\chi^{(2)}$ of 2D Te increases extraordinarily with increasing wavelength and reaches up to 5.58 nm V^{-1} at ≈2300 nm, which is the best infrared performance among the reported 2D nonlinear materials. Large $\chi^{(2)}$ of 2D Te also enables the high-intensity sum-frequency generation with an ultralow continuous-wave (CW) pump power. Theoretical calculations reveal that the exceptional performance is attributed to the presence of large BCD located at the Weyl points of 2D Te. These results unravel a new linkage between Weyl semiconductor and strong optical nonlinear responses, rendering 2D Te a competitive candidate for highly efficient nonlinear 2D semiconductors in the infrared region.

1. Introduction

2D Te ($P3_121$), formed by the stacking of 1D triple helix chain of Te atoms, has drawn great attention in recent years due to its high hole mobility[1,2] and high near-infrared (NIR) photo detectivity.[3,4] Recently, the topological property in quantum Hall sequences has been detected in the semiconducting 2D Te, which proves the existence of Weyl fermions near the Weyl nodes of 2D Te,[2,5] making it the first reported Weyl semiconductor. It is absolutely fascinating to explore other possible topological properties in this Weyl semiconductor. For instance, in Weyl semimetals, the large Berry curvature dipole (BCD) near the Weyl nodes will give rise to stronger nonlinear optical responses, which has been predicted by ab initio calculations[6] and verified experimentally in 3D TaAs.[7] However, no such study has been done in Weyl semiconductors, especially the newly

Q. Fu, B. Yao, M. Xu, Y. Deng, C. Zhu, X. Wang, L. Kang, Q. Zeng, B. Tang, Z. Dong, Z. Liu
School of Materials Science and Engineering
Nanyang Technological University
Singapore 639798, Singapore
E-mail: z.liu@ntu.edu.sg

Q. Fu, X. Wang, Q. Wang, B. K. Tay, Z. Liu
IRL 3288 CINTRA (CNRS-NTU-THALES Research Alliances)
Nanyang Technological University
Singapore 637553, Singapore

X. Cong, M.-L. Lin, P.-H. Tan
State Key Laboratory of Superlattices and Microstructures
Institute of Semiconductors
Chinese Academy of Sciences
Beijing 100083, P. R. China
E-mail: phtan@semi.ac.cn

X. Xu, J. Yang, X. Li
School of Materials Science and Engineering
Harbin Institute of Technology
Harbin 150001, P. R. China
E-mail: lxj0218@hit.edu.cn

S. Zhu, Q. Wang
School of Electrical & Electronic Engineering
Nanyang Technological University
50 Nanyang Avenue, Singapore 639798, Singapore
E-mail: qjwang@ntu.edu.sg

X. Zhao
School of Materials Science and Engineering
Peking University
Beijing 100871, P. R. China

S. Liu, Q. Wang
Division of Physics and Applied Physics
School of Physical and Mathematical Sciences
Nanyang Technological University
Singapore 637371, Singapore

The ORCID identification number(s) for the author(s) of this article can be found under https://doi.org/10.1002/adma.202306330

DOI: 10.1002/adma.202306330

discovered 2D Te. As a result, it is of great importance to explore the nonlinear optical properties of the Weyl semiconductor 2D Te and the influence of BCD on it.

Second-harmonic generation (SHG) is one of the most studied applications to evaluate the nonlinear optical responses of materials,[8–11] which requires a broken inversion symmetry.[12–16] However, this mainly exists in samples with specific layers for most 2D materials, such as odd-layer MoS_2 and even-layer $PdSe_2$.[1,17] Besides, although the infrared (IR) optics plays a significant role in real-world sensing applications, the overall SHG performances of 2D materials in the NIR region are poor and unsatisfactory.[8,9,12,13,17] Hence, it is urgently demanded to discover novel 2D materials with a high SHG performance in the NIR and even mid-infrared (MIR) region. As for 2D Te, due to its unique triple helix structure ($P3_121$), intrinsic broken inversion symmetry exists in 2D Te samples regardless of the thickness.[18] Moreover, 2D Te has a narrow energy bandgap and shows excellent photoresponse performance in the MIR region.[3,4] Therefore, it is believed that 2D Te should be a highly competitive candidate for MIR SHG applications.[19]

Here, 2D Te nanosheets were first synthesized and their anisotropic crystallographic orientation was demonstrated by angle-resolved polarized Raman spectroscopy. Strong SHG signals were obtained from the 2D Te flake where the $\chi^{(2)}$ of 2D Te is up to 23.3 times higher than that of monolayer MoS_2 over the range of 700 to 1500 nm.[20] Remarkably, $\chi^{(2)}$ of 2D Te shows a spectacular increasing trend (0.082–5.58 nm V^{-1}) from visible to MIR region (2300 nm), which is distinctive from other 2D semiconductors. Notably, the peak value of $\chi^{(2)}$ (5.58 nm V^{-1} at ≈2300 nm) is among the highest of the reported 2D nonlinear optical crystals, especially in the MIR region.[10,13,17] Hence, SFG signals can also be acquired with a low-power continuous-wave (CW) excitation. Theoretical calculations provide a proof-of-principle demonstration that this outstanding performance stems from the large BCD near the Weyl points of 2D Te. This work sheds light on the strong relationship between the Weyl semiconductor and nonlinear optical properties and more and more topological nonlinear materials to be discovered and play a significant role in the nonlinear optics related applications.

F. Liu
School of Optoelectronic Science and Engineering
University of Electronic Science and Technology of China
Chengdu 610054, P. R. China
Q. Xiong
State Key Laboratory of Low-Dimensional Quantum Physics and Department of Physics
Tsinghua University
Beijing 100084, P. R. China
Q. Xiong
Beijing Academy of Quantum Information Sciences
Beijing 100193, P. R. China
J. Zhou
Key Lab of advanced optoelectronic quantum architecture and measurement (Ministry of Education)
Beijing Key Lab of Nanophotonics & Ultrafine Optoelectronic Systems and School of Physics
Beijing Institute of Technology
Beijing 100081, P. R. China
Z. Liu
Institute for Functional Intelligent Materials
National University of Singapore
Blk S9, Level 9, 4 Science Drive 2, Singapore 117544, Singapore

2. Results and Discussion

2.1. Anisotropic Property of 2D Te

The α-phase Te (**Figure 1**a; Figure S1a,b, Supporting Information) belongs to the space group [152], $P3_121$, where Te atoms form a triple helix (3_1 symmetry) 1D chain. Along the z direction, 2D Te is formed by stacking of the 1D chains via van der Waals force, where an intrinsic broken inversion symmetry exists in this trigonal structure. The atomic structure of 2D Te was revealed by an aberration-corrected high-angle annular dark-field (HAADF) STEM imaging (Figure 1b). The corresponding fast Fourier transform pattern (FFT, Figure 1c) matches well with the one generated from crystal data (Figure S1c, Supporting Information, viewed from [120] direction),[21] which affirms the trigonal point group. As the atomically resolved imaging of 2D Te (Figure 1b) is highly consistent with the crystal structure from [120] direction (Figure S1b, Supporting Information), it can be confirmed that the crystal face of 2D Te is along the x-z plane, where the long edge in the optical image (Figure S1d, Supporting Information) is z direction. Two interplane spacings were measured to be 0.22 and 0.60 nm, corresponding to the $(\bar{2}10)$ and (001) planes, which coincide with the reported data.[1]

The anisotropic crystallography orientation of the 2D Te flake can be characterized by angle-resolved polarized Raman spectroscopy. In parallel polarization configuration (refer to Experimental Section), the angle (θ) between the crystal orientation (x) and the polarization direction of laser was adjusted by rotating a half-wave plate (HWP), which changed both polarization directions of the laser and Raman signal. In the symmetry of D_3^4, three Raman-active modes (one A_1 and two E modes – E_1(TO) and E_2) can be observed in Figure 1d and Figure S2 (Supporting Information), where the LO component of E_1 mode is absent due to destructive interference between the deformation potential and electro-optic contribution.[22] The polarized Raman intensity can be analyzed by the Raman tensors, $\boldsymbol{R}$, where the A_1 and E modes can be described as follows:[22,23]

$$\mathbf{R}\ (\mathrm{A}_1) = \begin{pmatrix} a & 0 & 0 \\ 0 & a & 0 \\ 0 & 0 & b \end{pmatrix},\ \mathbf{R}\ (\mathrm{E}(x)) = \begin{pmatrix} c & 0 & 0 \\ 0 & -c & d \\ 0 & d & 0 \end{pmatrix},\ \mathbf{R}\ (\mathrm{E}(y)) = \begin{pmatrix} 0 & -c & -d \\ -c & 0 & 0 \\ -d & 0 & 0 \end{pmatrix} \quad (1)$$

In our measurement configuration, the Raman intensity is evolved into: $I \propto \sum_j |e_R \cdot \mathbf{M} \cdot \mathbf{R}_j \cdot \mathbf{M}^{\mathrm{T}} \cdot e_L|^2$,[24] where $\boldsymbol{M}$ refers to the transform matrix and $\boldsymbol{M}^T$ indicates transposition of $\boldsymbol{M}$, and $e_L^T = (1\ 0\ 0)$ and $e_R = (1\ 0\ 0)$ indicates incident and collected light polarization vectors along x axis, respectively (refer to Figure S2, Supporting Information). Due to absence of LO component, the Raman intensity of E_1(TO) mode involves $\boldsymbol{R}(E(x))$, while that of E_2 mode involves $\boldsymbol{R}(E(x))$ and $\boldsymbol{R}(E(y))$. Thus, the Raman intensities of A_1, E_1(TO) and E_2 modes under parallel polarization configuration ($I_{\parallel}$) as a function of θ can be given as: $I_{\parallel}(\mathrm{A}_1) \propto |a\cos^2(\theta) + b\sin^2(\theta)|^2$, $I_{\parallel}(\mathrm{E}_1(\mathrm{TO})) \propto |c\cos^2(\theta)|^2$,

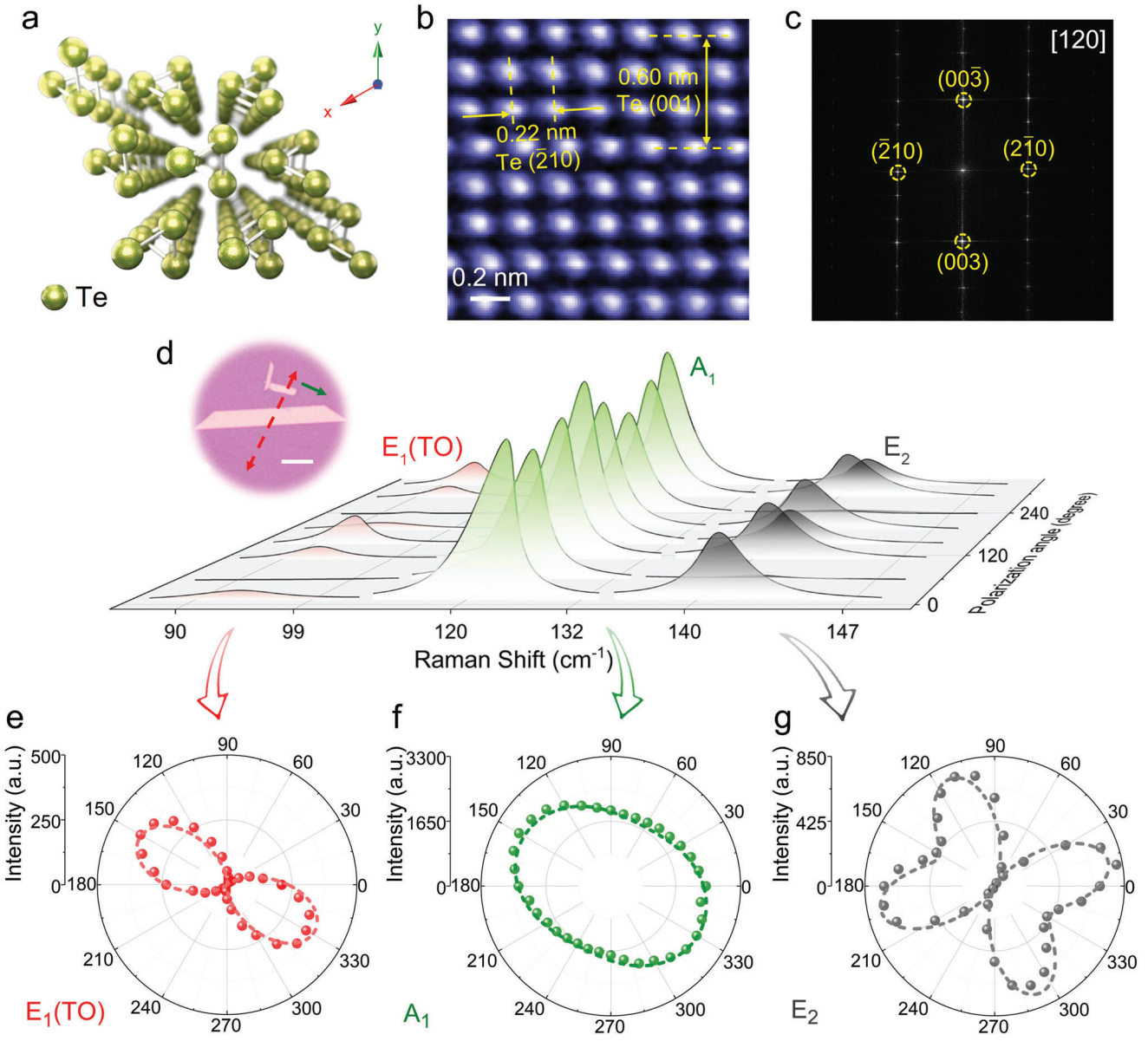

Figure 1. Anisotropic property of 2D Te. a) Crystal structure of 2D Te along *z* direction view. b) Atomically resolved HAADF-STEM image of 2D Te. c) FFT pattern of (b), confirming the zone axis of [120]. d) Angle-resolved polarized Raman spectra of 2D Te with the parallel configuration. Inset: Optical image of 2D Te shows the initial polarization direction of laser (red dashed arrow) in the Raman spectrum test while the rotation direction is marked out by the green solid arrow. Scalebar: 20 µm. e–g) The polarization dependence of E_1(TO) (e), A_1 (f), and E_2 (g) peaks intensity, respectively. The strongest signals were acquired at the polarization parallel to *x* direction for both E_1(TO) and A_1 peaks.

$I_{\parallel}(E_2) \propto |c\cos^2(\theta)|^2 + |2d\cos(\theta)\sin(\theta)|^2$. As shown in Figure 1e–g, the angle-resolved Raman intensities of E_1(TO), A_1 and E_2 modes can be well fitted accordingly. The initial polarization direction of the laser with respect to the sample is marked out in the inset of Figure 1d. Therefore, the Raman intensities of E_1(TO) and A_1 peaks reach their maximum at the polarization direction parallel to the *x* direction (Figure S1d, Supporting Information), which can be used to determine the crystallography orientation of 2D Te flakes. In addition, the angle-resolved Raman spectra intensities under the perpendicular polarization configuration (refer to Experimental Section) were also obtained (Figure S3, Supporting Information). All three vibration modes show a four-lobe shaped polarization dependence, in agreement with corresponding theoretical analysis using the same Raman tensor elements.

2.2. SHG and Large Second-Order Nonlinear Susceptibility

Due to the triple helical chain-like structures, Te with arbitrary thickness is expected to process high optical anisotropy, broken inversion symmetry and gigantic static SHG coefficient.[18] Although the nonlinear optical properties of both bulk (3D)[25–27]

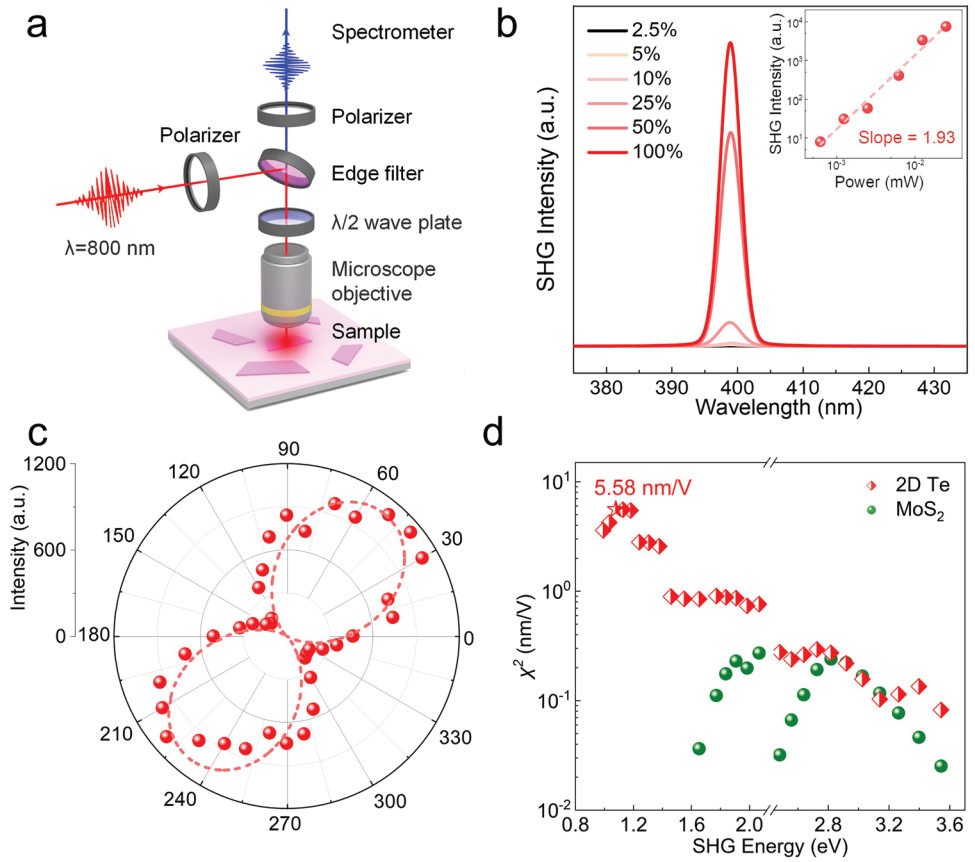

Figure 2. SHG performance of 2D Te. a) Schematics of a back-reflection SHG measurement setup. b) Power-dependent SHG spectra of 2D Te (Pump power at 100%: 0.031 mW). A typical peak at 400 nm was obtained, which is exactly the double-frequency position of the fundamental wavelength (800 nm). Inset: the linear fitting of SHG intensity over power density in a logarithmic manner, revealing a slope of ≈1.93. c) Angle-resolved polarized SHG spectra, presenting a two-lobe shaped polarization dependence. The strongest signal shows out at the *x* direction. d) Second-order nonlinear optical susceptibilities of 2D Te (700 nm to 2500 nm) and monolayer MoS_2 (700 to 1500 nm). The peak value of 2D Te is 5.58 nm V^{-1} at ≈2300 nm, marked out with the star symbol.

and nanowire (1D) forms[28,29] of Te have been reported, as a novel Weyl semiconductor, the application of 2D Te in nonlinear optics has not been examined experimentally yet. To test the SHG performance of 2D Te (10 nm thick sample, Figure S4a, Supporting Information), a pulsed laser with a wavelength of 800 nm was utilized as a pump source and the signals were collected in a back-reflection geometry with a parallel configuration (**Figure 2**a and Experimental Section). Figure 2b displays the SHG spectra of 2D Te with the peak located at 400 nm, which corresponds to frequency doubling signal of the excitation wavelength (800 nm). Besides, the power dependence of the SHG intensity (inset Figure 2b, logarithmic manner), which helps further identify the order of nonlinear process, exhibits a quadratic dependence with a slope of ≈1.93 (close to 2). Both results indicate that this is a second-order nonlinear process.[8] The polarization-dependent SHG was studied by rotating the sample under the parallel configuration ($I_{\parallel}$). Figure 2c shows the polarized SHG intensities of 2D Te, which exhibits an obvious dependence on θ. The angle-dependent SHG intensity can be analyzed by the second-order nonlinear susceptibility tensor ***d***. According to the crystalline symmetry (D_3^4) of 2D Te and the ab initio calculations,[23] there are only two independent nonzero elements, and the SH polarizations ***P*** can be given by:

$$\begin{bmatrix} P_x(2\omega) \\ P_y(2\omega) \\ P_z(2\omega) \end{bmatrix} = 2\varepsilon_0 \cdot \mathbf{d} \cdot \mathbf{E}^2 = 2\varepsilon_0 \begin{bmatrix} d_{11} & -d_{11} & 0 & d_{14} & 0 & 0 \\ 0 & 0 & 0 & 0 & -d_{14} & -d_{11} \\ 0 & 0 & 0 & 0 & 0 & 0 \end{bmatrix} \begin{bmatrix} E_x(\omega)E_x(\omega) \\ E_y(\omega)E_y(\omega) \\ E_z(\omega)E_z(\omega) \\ 2E_y(\omega)E_z(\omega) \\ 2E_x(\omega)E_z(\omega) \\ 2E_x(\omega)E_y(\omega) \end{bmatrix} \quad (2)$$

where d_{ij} is the element of the dielectric susceptibility tensor, ϵ_0 is permittivity of free space, E is electric field intensity of the incident light. In the case of parallel configuration, electric field components should be: $E_x(\omega) = E_0 \cos(\theta)$, $E_y(\omega) = 0$, $E_z(\omega) = E_0 \sin(\theta)$, and the SHG intensity is $I_{\parallel}(SHG) \propto (P_x \cos(\theta) + P_z \sin(\theta))^2 = d_{11}^2 \cos^6(\theta)$. Thus, the intensity of SHG signals as a function of θ is expected to exhibit a two-petal shaped polarization dependence. As shown in Figure 2c, the experimental data can be well fitted via the above-mentioned nonlinear function, demonstrating the high consistency between the theoretical and experimental data. According to the initial polarization direction of laser (Figure S4b, Supporting Information),

the strongest SHG signal was obtained at the direction parallel to the *x* direction of 2D Te, which is same with the analysis of A_1 and E_1(TO) Raman intensities. In addition, the polarization direction of incident laser can also be controlled via adjusting the HWP, while the sample was anchored and all SHG signals with arbitrary polarization direction were collected. For such case, $I_{\parallel}(SHG) \propto (P_x + P_z)^2 = d_{11}^2 \cos^4(\theta)$, and the experimental data also display a two-lobe shaped polarization dependence of SHG intensity (Figure S4c, Supporting Information).

According to the theoretical calculations, 2D Te not only has a large value of $\chi^{(2)}$ in the whole IR range (0.4–1.8 eV),[18] but also $\chi^{(2)}$ increases substantially from the visible to NIR and MIR region. To investigate the $\chi^{(2)}$ value of 2D Te, SHG spectra of 2D Te and monolayer MoS_2 (H phase) in a wide excitation region (700–1500 nm) were measured on fused silicate substrate, as shown in Figure 2d and Figure S5a (Supporting Information). The quadratic dependence (Figure S5b, Supporting Information, slope of 1.91 and 1.90) confirms signals of both 2D Te and MoS_2 are from second-order nonlinear processes. In Figure S5 (Supporting Information), when excitation wavelength increases from 700 to 1500 nm, the normalized SHG intensity of monolayer MoS_2 first increases and then declines, reaching its maximum at the excitation wavelength of 850–880 nm, which matches well with previous reports.[20,30] Note that when the excitation wavelength is larger than 1500 nm, the SHG signal of MoS_2 is too weak to collect. In contrast, the SHG intensity of 2D Te is much stronger than that of monolayer MoS_2 and keeps increasing from 700 to 1500 nm. The $\chi^{(2)}$ of both materials are obtained from normalized SHG intensity with the reference of a *z*-cut quartz using the equation:[30,31]

$$\frac{|\chi_S^2|}{\left|\chi_{quartz,11}^2\right|} = \frac{c}{4\omega d_s\left(n(\omega) + n(2\omega)\right)} \cdot \sqrt{\frac{I_S}{I_{quartz}}} \quad (3)$$

where χ_S^2 and d_s is the sheet susceptibility and thickness of measured samples, and $\chi_{quartz,11}^2$ is bulk susceptibility value of z-cut quartz along its d_{11} direction (taken to be 0.6 pm V^{-1} and constant across the wavelength range of our measurements). $n(\omega)$ and $n(2\omega)$ are the refractive indexes of the fused silica at pump and second harmonic wavelengths, respectively, and *c* is speed of light in vacuum. I_S and I_{quartz} are SHG intensities measured on the samples and z-cut quartz (both normalized to the square of pump power). The $\chi^{(2)}$ of monolayer MoS_2 ranges from 0.025 to 0.24 nm V^{-1}, showing high consistency with the reported values.[20] In comparison, the $\chi^{(2)}$ of 2D Te is ≈0.082–0.90 nm V^{-1}, which is up to 23.3 times higher than that of monolayer MoS_2 at the excitation wavelength of 1500 nm. Thickness dependent SHG measurement shows a positive relationship between the intensity and the thickness since 2D Te has the intrinsic broken inversion symmetry regardless of the thickness (Figure S6, Supporting Information).

The ultrahigh MIR sensing performance and the unusual increase of $\chi^{(2)}$ in the MIR region drives us to further extend the excitation wavelength to MIR region (2.5 μm). As displayed in Figure 2d, $\chi^{(2)}$ of 2D Te increases slowly from the visible region (700 nm) to the NIR region (1.7 μm), and then increases drastically in MIR region (2.3 μm). Such energy dependent $\chi^{(2)}$ has never been reported in other 2D nonlinear optical materials as they show lower SHG responses in MIR region. A peak value of 5.58 nm V^{-1} can be found at the excitation wavelength of ≈2300 nm. In comparison with the reported $\chi^{(2)}$ of 2D materials (**Table 1** and Figure S7, Supporting Information),[3,5,6,7,10,20,32] the remarkably high $\chi^{(2)}$ of 2D Te makes it one of the most efficient 2D nonlinear optical materials, especially in the MIR range. The conversion efficiency of SHG can be estimated using the equation $\eta_{2\omega} = P_{SHG}(2\omega)/P_1^2(\omega)$,[33] where $P_{SHG}(2\omega)$ and $P_1(\omega)$ are the power of SHG signal and intrinsic excitation light, respectively. The estimated efficiency is ≈1.6×10^{-3} W^{-1}, which is larger than that of MoS_2, GaSe and $NbOI_2$ flake.[34–36]

Table 1. Comparison of second-order nonlinear optical susceptibilities of 2D semiconductors.

2D Semiconductors	$\chi^{(2)}$ [nm V^{-1}]	Fundamental wavelength [nm]	Thickness	Reference
2H-MoS_2	0.25	870	1L	[20]
2H-$MoTe_2$	2.5	1550	1L	[32]
2H-WS_2	0.002	800	1L	[14]
ϵ-InSe	0.013	800	≈20 nm	[14]
ReS_2	0.9	1558	2L	[12]
$PdSe_2$	0.0517	880	4L	[17]
GaSe	2.4	1210	1L	[9]
InSe	6.39	800	1L	[13]
2D Te	5.58	2300	≈10 nm	This Work

Note: 1L, 2L, 4L stand for monolayer, bilayer, tetralayer, respectively.

2.3. SFG and the Power, Wavelength, and Polarization Dependence

To further explore large $\chi^{(2)}$ of 2D Te, the power-, wavelength-, and polarization-dependent sum-frequency generation (SFG) signals were measured, which was generated under the excitation of two CW lasers with different wavelengths. Although the pump irradiances are more than three orders of magnitude lower than that of typical pulsed excitation condition, SHG and SFG spectra with high intensity can be obtained due to the large $\chi^{(2)}$. In **Figure 3**a, two incident lasers with wavelength λ_1 (850 nm) and λ_2 (1064 nm) can generate SHG1 (425 nm, $\lambda_1/2$) and SHG2 ($\lambda_2/2$, 532 nm) and SFG ($\frac{\lambda_1\lambda_2}{\lambda_1+\lambda_2}$, 472 nm) signals. As shown in Figure 3b,c, when the power of λ_2 (1064 nm) was fixed at 3.6 mW, the intensity of SHG1 (425 nm) and SFG (472 nm) as a function of λ_1 (850 nm) power exhibits linear dependence (logarithmic manner) with a slop of ≈1.94 and ≈0.98, respectively, confirming the corresponding processes. Also, the relative intensity of the SFG signal to the SHG1 signal could be regulated via tuning the power density of the excitation light. For example, the maximum ratio of the SFG signal over the SHG1 signal in Figure 3a could be up to 6. Figure 3d presents the result of wavelength-dependent measurement where λ_1 was tuned from 750 to 1000 nm with a step of 50 nm and λ_2 was fixed at 1064 nm. It is obvious that when λ_1 is changed, the location of SFG peak shifts accordingly. Besides, the high intensity of SFG signal in the whole region of λ_1 confirms the large $\chi^{(2)}$ in a wide range, which further indicates the promising application in nonlinear optical devices. Finally,

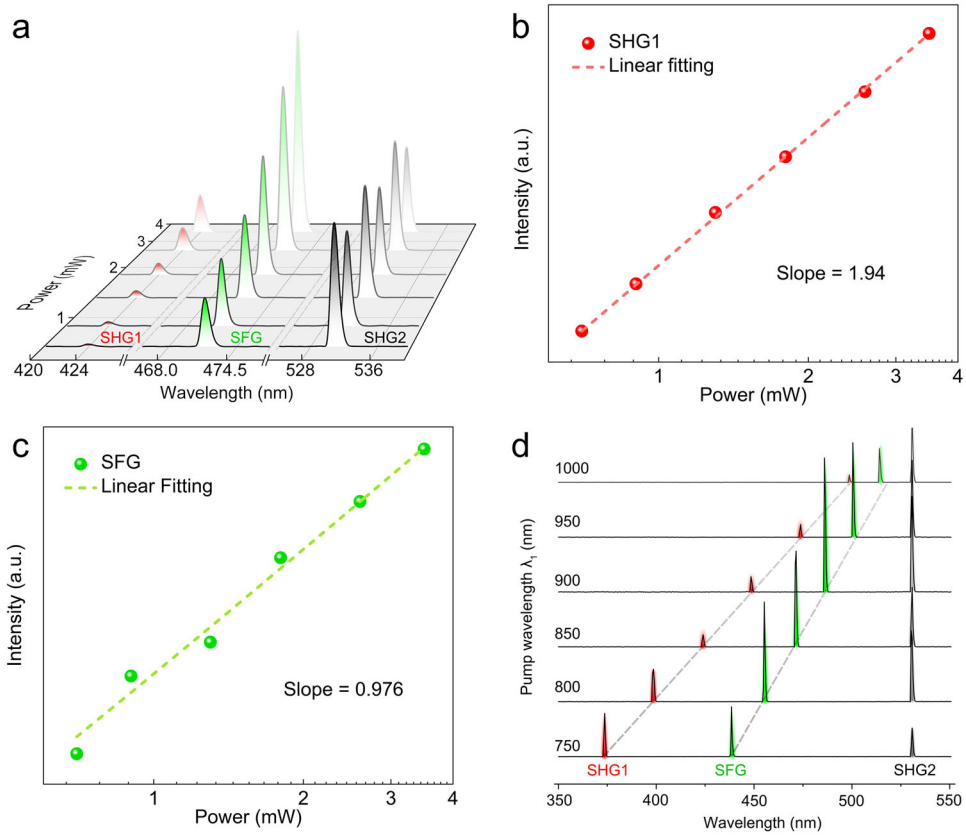

Figure 3. Sum-frequency generation of 2D Te. a) The power-dependent SFG spectra of 2D Te. b–c) The linear fitting of SHG1 (b) and SFG (c) intensities in a) over power density in a logarithmic manner, revealing a slope of ≈1.94 and 0.98, respectively. d) The wavelength-dependent SFG spectra of 2D Te.

Figure S8 (Supporting Information) presents angle-resolved polarized SFG signals (Figure S8b, Supporting Information), which shows a two-petal intensity distribution, same with that of SHG signals (Figure S8a,c, Supporting Information).

2.4. Density Function Theory Calculation

To reveal the nature of the giant SHG, the correlation between nonlinear optical property and topological electronic structure of Te has been theoretically investigated using the-art-of-state density function theory (DFT). Te is a Weyl semiconductor with tens of Weyl nodes near Fermi level in the whole Brillouin zone. **Figure 4**a shows the band structure of Te, where the Weyl points on the four subbands (c_2, c_1, v_1 and v_2) near Fermi level are labelled with red dots. The band gap is determined as 0.28 eV, close to the experimental measurements (0.31 eV).[2] Te is not a strong topological insulator with $Z_2 = 0$,[37] while the two bands (c_1 and v_1) have nontrivial topology, of which the Chern number is $C = 1$ and $C = -1$, respectively. The transition dipole moment (TDM) is analyzed to reveal the capability of the optical transition of excited electrons, as shown in Figure S9 (Supporting Information). Along the high symmetric k-path, the optical transition peaks contributed by the four subbands are primarily located at the position of Weyl points which play an important role in optical absorption process. However, the role of Weyl points in optical nonlinear response of such Weyl semiconductors remains unclear.

The analogue systems with Weyl topology, Weyl semimetals, have been extensively predicted to be excellent candidates as nonlinear optical materials, owing to the large Berry curvature which can describe the nonlinear optical response from semiclassical picture.[38] For a linearly polarized light, SHG is described by the second-harmonic current response $j_a^{2\omega} e^{2i\omega t}$, where $j_a^{2\omega} = \chi_{abc}\, \varepsilon_b \varepsilon_c$. The nonlinear conductivity tensor χ_{abc} reads,[38]

$$\chi_{abc} = -\epsilon_{adc} \frac{e^3 \tau}{2(1 + i\omega\tau)} \int_k f_0 \left(\partial_b \Omega_d\right) \tag{4}$$

where ϵ_{adc} is the third-rank Levi–Civita symbol, τ refers to the relaxation time approximation, Ω_d is the berry curvature and f_0 is the equilibrium Fermi–Dirac distribution. It is concluded that the nonlinear conductivity tensor is proportional to Berry curvature dipole (BCD) defined as,[34]

$$D_{bd} = \int_k f_0 \left(\partial_b \Omega_d\right) \tag{5}$$

The Berry curvature dipole in non-centrosymmetric materials is the origin to induce nonlinear Hall effect, which have already been used to understand the underlying mechanism of the second-harmonic generation (SHG) in topological insulators and Weyl semimetals.[6]

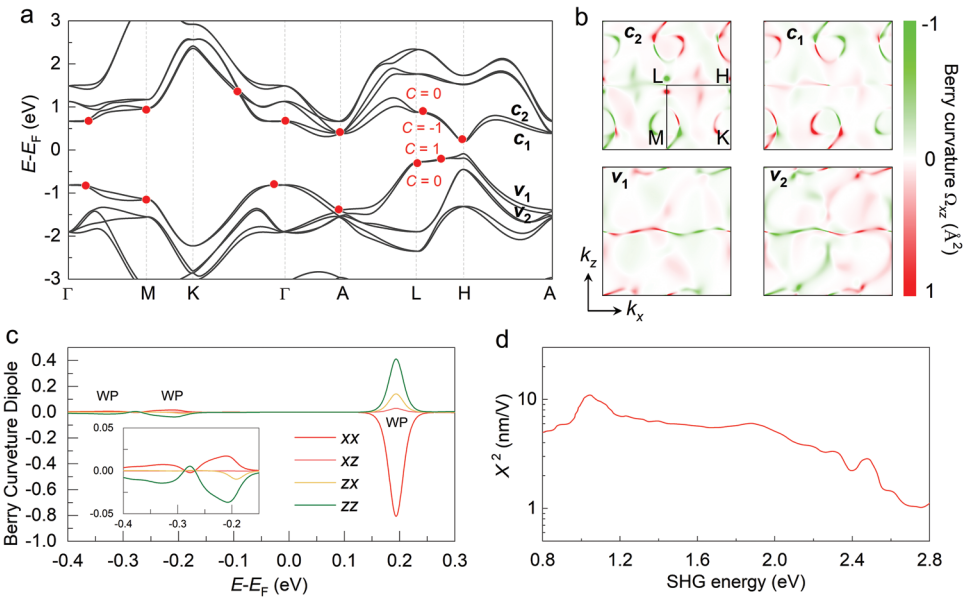

Figure 4. Contribution of topology to the second-order nonlinear optical response of Te. a). Band structure constructed using Wannier function, where the red dots indicate the position of Weyl points on the c_2 (Chern munber $C = 0$), c_1 (Chern munber $C = -1$), v_1 (Chern number $C = 1$) and v_2 (Chern number $C = 0$) subbands. b). The distribution of Berry curvature Ω_{zx} of the four subbands on $k_y = 0.5$ plane, of which the intensity is normalized. c). Energy-dependent Berry curvature dipole of the component D_{xx}, D_{xz}, D_{zx}, and D_{zz}. The inset is to highlight the contribution of the Weyl points to the Berry curvature dipole within the energy range from −0.4 eV to −0.15 eV. d). The theoretical result of second-order nonlinear optical susceptibility of Te.

The semiclassical concept and the DFT scheme were combined to unveil the nature of giant SHG in Te. To obtain the topological character, the normalized Berry curvatures Ω_{zx} on $k_y = 0.5$ plane of c_2, c_1, v_1 and v_2 subbands are depicted in Figure 4b. The intensity of Berry curvature is quite robust with chiral symmetric distribution. The line-shape peaks originate from nodal-line-like band anti-crossing, whereas dot peaks are determined by the Weyl points. The Berry curvature of the two occupied bands and the two unoccupied bands presents opposite phases, except the dot pairs on c_2 and v_2 subbands. Due to the robust Berry curvature, Te yields a large intrinsic anomalous hall effect, as shown in Figure S10 (Supporting Information). As observed from the energy-dependent anomalous hall conductivities in *xy*-, *yz*- and *zx*-plane, the resonant peaks are primarily contributed by the Weyl points which locate at 0.19 eV at H point, −0.20 eV at L-H path and −0.28 eV at L point. Because of the topological non-invariant $Z_2 = 0$ (see the Wilson loop in Figure S11, Supporting Information), the gap is not closed in the anomalous hall conductivity spectra. By contrast, the response of nonlinear Hall effect in *yz*- and *zx*-plane is much stronger than that in *xy*-plane.

Based on the Equation 5, the BCD derived from the Berry curvature of all bands was further obtained. Due to the lack of inversion symmetry, non-zero BCD component can be expected. The BCD projections D_{xx}, D_{xz}, D_{zx} and D_{zz} are shown in Figure 4c. Around the Weyl points, the BCD is obviously enhanced, which demonstrates that the Weyl points are indeed the origin of the second-order nonlinear response (see Equation 4), especially the Weyl point at 0.19 eV at H points. Component D_{xx} and D_{zz} are relatively larger in comparison with D_{xz} and D_{zx}. According to Equation 4, D_{xx} and D_{xz} correspond to χ_{xxx}; D_{zz} and D_{zx} correspond to χ_{zzz}. Using Wannier function method, we build the tight-binding Hamiltonian for Te and reproduce the band structure of DFT. Based on the obtained Hamiltonian, the nonlinear optical calculation is realized, as shown in Figure 4d. The $\chi^{(2)}$ tensor performs a great match with our experimental measurement (Figure S12, Supporting Information). The peak value of our prediction proves that Te indeed has a stronger second-order nonlinear response in NIR and MIR optical region, which is determined by the Weyl points near the bandgap. Theoretical calculation of the contribution from the dipole to the nonlinear properties was also conducted, unlike the traditional SHG materials with a strong polarization, there is no electric dipole in Tellurium, as shown in Figure S13 (Supporting Information). Thus, the giant SHG is primarily attributed to the intrinsic topology of electronic structure in Tellurium. Although the robust SHG can be well understood using the semiclassical concept in combination with DFT, the direct connection between the topology and nonlinear optical response needs to be built with more efforts in the future.[39]

3. Conclusion

In summary, giant second-order optical responses of 2D Te originated from the large Berry curvature dipole near the Weyl points have been demonstrated. Angle-resolved polarized Raman spectra have revealed the anisotropic crystal orientation of 2D Te. Second-order optical properties of 2D Te have been studied systematically (light power density, polarization angle, wavelength). As compared, $\chi^{(2)}$ of 2D Te is up to 23.3 times higher than that of MoS_2 over the range of 700 to 1500 nm. Moreover, $\chi^{(2)}$ of 2D Te exhibits an exceptional increase from 700 to 2300 nm and a peak value of 5.58 nm V^{-1} was acquired, which shows highest infrared performance among the reported 2D materials. High-intensity SFG signals have also been obtained under different polarizations, laser powers, and wavelengths with a low-power CW

laser excitation. First-principle calculations unveil that the origin of these strong nonlinear optical responses is the large Berry curvature dipole near the Weyl points of 2D Te. This work paves the way for exploring more 2D Weyl semiconductors and their superior nonlinear optical properties.

4. Experimental Section

Synthesis and Characterization of 2D Te: In the hydrothermal synthesis of 2D Te, 37.5 mg of PVP-55 and 23 mg of $NaTeO_3$ were mixed and dissolved in 8 mL of DI water in a 50 mL Teflon-lined stainless autoclave. 0.83 mL of $NH_3{\cdot}H_2O$ solution and 0.42 mL of hydrazine monohydrate solution were then added into the solution subsequently. The autoclave was ultrasound sonicated for 30 min before sealed and placed in an oven. The autoclave was then heated to 180 °C and held for 4 h, then cooled down to room temperature naturally. The as-grown 2D Te was dispersed in 40 mL of DI water and centrifuged at 10000 rpm for 7 min, repeated three times. The final product was dispersed in absolute ethanol by ultrasound sonication and transferred to the target substate by spin-coating (Silicon and fused silicate substrate) and dip-coating (Mo grid). AFM was conducted under the Asylum Research Cypher Scanning Probe Microscope system with a tapping mode. HAADF-STEM imaging was carried out on an aberration-corrected JEOL ARM-200F equipped with a cold field emission gun, operating at 80 kV, and an ASCOR probe corrector. The convergence semi-angle of the probe was set at ≈30 mrad while the collection semi-angle ranges from about 68 to 280 mrad. A dwell time of 19 µs $pixel^{-1}$ was set for single-scan imaging.

Angle-Resolved Polarized Raman Spectroscopy Analysis of 2D Te: Angle-resolved polarized Raman spectra were obtained by a Jobin–Yvon HR-Evolution micro-Raman system with the laser of 532 nm laser (a 100× objective lens (numerical aperture = 0.9) and grating of 1800 lines mm^{-1}). The parallel/perpendicular configuration refers to the polarization of the polarizer at the incident light path was parallel/perpendicular to that of the analyzer placed before the spectrometer. A HWP was placed in the common optical path of incident and scattered light propagation. The laser beam propagates through a HWP, while the scattered Raman signal travels back and its polarization was also rotated by the same half-wave plate. The angle between the crystal orientation and the first polarizer was adjusted by rotating the HWP.

SHG and SFG Measurement: Two sets of pulsed lasers were utilized to measure the SHG. The first pulsed laser using a mode-locked Ti/Sapphire oscillator as the pumping source at 800 nm wavelength (80 MHz, 100 fs) was utilized. The polarization-dependent SHG was measured in a back-reflection geometry and the direction of the incident polarizer parallels to that of the collection analyzer, where only SHG signal parallel to the polarization of incident laser can be detected. Power-dependent spectra were obtained under the excitation of laser with different power densities. To control the polarization angle, one method was to rotate the sample and the other was to rotate the HWP in the common optical path of incident and scattered light propagation. To compare the wavelength-dependent SHG performance, the other optical parametric amplifier system (≈150 fs, 100 kHz) was used as a pump source. 2D Te and monolayer MoS_2 were transferred onto fused silicate substrate and SHG signals were obtained in ambient environments with laser in the region of 700 to 1500 nm (MoS_2) and 2500 nm (2D Te) which were normalized by the SHG signal of z-cut quartz with corresponding wavelength. To acquire SFG signal, two continuous-wave lasers with different wavelengths were employed. In the power-dependent SFG measurement, the power of one laser (1064 nm) was fixed at 3.6 mW, while that of the other (850 nm) was adjusted from 0.7 to 3.5 mW. In the wavelength-dependent SFG measurement, the wavelength of one laser was fixed at 1064 nm, while that of the other was adjusted from 750 to 1000 nm. In the angle-resolved SFG test, the polarization directions of the incident lasers were tuned by adjusting the half-wave plate, while the sample was anchored. For SHG and SFG measurements in the excitation range of 650–1050 nm, a 50× long-working-distance objective lens (NA = 0.5) was used, with an input beam size of ≈1–2µm. The ultrafast laser had a repetition rate of ≈80 MHz and a pulse duration of ≈100 fs. To avoid laser heating effects, we ensured that the peak power at all wavelengths was kept below 5 mW.

First-Principle Calculation: Density functional theory technique was employed to evaluate the electronic structure of Tellurium, using VASP package[40,41] based on the projector-augmented wave (PAW) pseudopotential and plane-wave basis set.[42,43] To accurately solve Kohn–Sham single-particle equation, the strongly constrained and appropriately normed (SCAN) meta-generalized gradient approximation (METAGGA) exchange-correlation potential was employed.[44] rVV10 function[45] was chosen to evaluate the weak van der Waals interaction among the spiral Te chains. With the criterion of absolute force on each atom less than 0.01 eV $Å^{-1}$, the lattice parameters were relaxed to $a = b = 4.71$ Å and $c = 5.84$ Å in a good agreement with our experimental measurement. A Gamma-centered k-point mesh of 15×15×11 and a cutoff energy of 500 eV were set for both the structural relaxation and self-consistent calculation. The spin-orbital coupling (SOC) was included to exam the topology of Te. Using maximally localized Wannier functions, the Hamiltonian of tight-binding Model was constructed using Wannier90 package[46] to reproduce the band structure of Te. The Z_2 topological invariant can be obtained from the constructed Wannier charge center defined as,[47]

$$\bar{x}_n = \frac{i}{2\pi}\int_{-\pi}^{\pi} \left\langle u_{nk}\left|\nabla_k\right|u_{nk}\right\rangle dk \tag{6}$$

where u_{nk} is the constructed Bloch function. Based on the Kubo formula approach,[48] the Berry curvature reads,

$$\Omega^{\gamma}_{n,\alpha\beta}(k) = Im\sum_{n'\neq n}\frac{\left\langle u(n,k)\left|\hat{v}_{\alpha}\right|u(n',k)\right\rangle\left\langle u(n,k)\left|\hat{v}_{\beta}\right|u(n',k)\right\rangle - (\beta-\alpha)}{\left(E(n,k)-E(n',k)\right)^2} \tag{7}$$

By summing Berry curvature over all valence bands, the anomalous Hall conductivity was obtained as,[48]

$$\sigma^{\gamma}_{\alpha\beta}(E_F) = \frac{e^2\hbar}{(2\pi)^3}\int_k dk\sum_{E(n,k)<E_F} f(n,k)\,\Omega^{\gamma}_{n,\alpha\beta}(k) \tag{8}$$

where $E(n, \mathbf{k})$ is the eigenvalue of the nth eigenstate of $|u(n, \boldsymbol{k})\rangle$ at the $\mathbf{k}$ point, $\hat{v}_{\alpha(\beta)} = (1/\hbar)(\partial H(k)/\partial k_{\alpha(\beta)})$ is the velocity operator, and $f(n, \mathbf{k})$ is the Fermi–Dirac distribution. The Chern number of the nth band was determined from the integration of corresponding Berry curvature over Brillouin zone,[49]

$$C^n = \frac{1}{2\pi}\int_{BZ}\Omega_n(k)\,dk \tag{9}$$

Based on the constructed Wannier Hamiltonian model, the Berry curvature dipole was obtained using Equation 5. In addition, derived from the constructed wavefunctions, the optical transition dipole moment was calculated by,

$$\mathrm{TDM}_{a\to b} = \frac{i\hbar}{(E_b-E_a)\,m}\left\langle\psi_a\left|\mathbf{p}\right|\psi_b\right\rangle = e\int\psi_b^*(\mathbf{r})\,\mathbf{r}\psi_a(\mathbf{r})\,d^3\mathbf{r} \tag{10}$$

where ψ_a and ψ_b are the wavefunctions of eigenstates E_a and E_b, respectively.

Calculation of Second-Order Harmonic Generation (SHG): Based on the Hamiltonian constructed by Wannier functions, we further calculate the SHG of Te using the developed code (ERETCAD). In principle, the second-order nonlinear susceptibility $\chi^{(2)}$ was composed of the interband contributions $\chi_e^{(2)}$ and mixed interband and intraband contributions $\chi_i^{(2)}$ defined as,[50]

$$\chi^{(2)} = \chi_e^{(2)} + \chi_i^{(2)} \tag{11}$$

Alternatively, the inter-band contribution was described as,

$$\chi_e^{(2)} = \frac{iC}{\omega_2 m} \sum_{n,m,l,k} \frac{p^c_{mn}}{\omega_{nm} - \omega_2} \left(\frac{r^b_{nl} r^a_{lm} f_{ml}}{\omega_{lm} - \omega_1} - \frac{r^a_{nl} r^b_{lm} f_{ln}}{\omega_{nl} - \omega_1} \right) \quad (12)$$

The mixed contribution was described as,

$$\chi_i^{(2)} = \frac{-C}{\omega_2 m} \sum_{n,m,k} \frac{p^c_{mn}}{\omega_{nm} - \omega_2} \left(\frac{r^a_{nm} f_{mn}}{\omega_{nm} - \omega_1} \right)_{;k^b} \quad (13)$$

where $C = e^3 K/\hbar^2 m$, K accounts for the usual factors l; r is the position operator; ω_{mn} is the frequency difference between band m and n; f is the Fermi–Dirac distribution functions; p is the polarization operator.

Supporting Information

Supporting Information is available from the Wiley Online Library or from the author.

Acknowledgements

Q.F. acknowledges the great help from J.Z. This work was supported by the National Key Research & Development Program (2021YFE0194200), Singapore NRF-CRP21-2018-0007 and NRF-CRP22-2019-0007, Singapore Ministry of Education via AcRF Tier 3 Programme "Geometrical Quantum Materials" (MOE2018-T3-1-002), A*STAR under its AME IRG Grant (Award No. A2083c0052). This research/project is supported by the Ministry of Education, Singapore, under its Research Centre of Excellence award to the Institute for Functional Intelligent Materials (Project No. EDUNC-33-18-279-V12). F.L. acknowledges support from the National Key Research & Development Program (2020YFA0309200). P.T. and M.L. acknowledge support from the National Natural Science Foundation of China (Grant Nos. 12004377, 11874350, and 12204472), the CAS Key Research Program of Frontier Sciences (Grant No. ZDBS-LYSLH004) and the Strategic Priority Research Program of CAS (Grant No. XDB0460000). B.T. acknowledges funding by Singapore MOE under a Tier 2 funding (MOE2019-T2-2-075). X.Z. thanks the support from the Presidential Postdoctoral Fellowship, Nanyang Technological University, Singapore via grant 03INS000973C150.

Conflict of Interest

The authors declare no conflict of interest.

Author contributions

Q.F., X.C., X.X., and S.Z. contributed equally to this work. Q.F., F.L., and Z.L. conceived and designed the research. Q.F. conducted the synthesis of 2D Te and the characterization under the supervision of Z.L.. X.Z. and B.Y. performed the STEM and TEM measurements and data analysis under the supervision of Z.L. and Z.D.. Q.F. and X.C. performed the angle-resolved polarized Raman spectroscopy under the supervision of P.T.. Q.F. and S.L. performed the power- and polarization-dependent SHG measurements under the supervision of Q.X.. Q.F., S.Z., X.C., and M.L. performed the wavelength-dependent SHG measurements of 2D Te and monolayer MoS_2 and the SFG measurements under the supervision of J.Z., Q.W., and P.T., X.X., and J.Y. conducted the DFT calculation under the supervision of X.L.. C.Z., Y.D., and F.L. contributed to the data analysis. Q.F., X.C., X.X., X.Z., and Z.L. prepared the figures. Q.F., X.C., X.X., P.T., and Z.L. prepared the manuscript with comments from all authors.

Data Availability Statement

The data that support the findings of this study are available from the corresponding author upon reasonable request.

Keywords

2D materials, Berry curvature dipoles, second-harmonic generation, tellurium, weyl semiconductors

Received: June 30, 2023
Revised: September 5, 2023
Published online: October 15, 2023

[1] Y. Wang, G. Qiu, R. Wang, S. Huang, Q. Wang, Y. Liu, Y. Du, W. A. Goddard, M. J. Kim, X. Xu, P. D. Ye, W. Wu, *Nat. Electron.* **2018**, *1*, 228.
[2] G. Qiu, C. Niu, Y. Wang, M. Si, Z. Zhang, W. Wu, P. D. Ye, *Nat. Nanotechnol.* **2020**, *15*, 585.
[3] M. Amani, C. Tan, G. Zhang, C. Zhao, J. Bullock, X. Song, H. Kim, V. R. Shrestha, Y. Gao, K. B. Crozier, M. Scott, A. Javey, *ACS Nano* **2018**, *12*, 7253.
[4] C. Shen, Y. Liu, J. Wu, C. Xu, D. Cui, Z. Li, Q. Liu, Y. Li, Y. Wang, X. Cao, H. Kumazoe, F. Shimojo, A. Krishnamoorthy, R. K. Kalia, A. Nakano, P. D. Vashishta, M. R. Amer, A. N. Abbas, H. Wang, W. Wu, C. Zhou, *ACS Nano* **2019**, *14*, 303.
[5] N. Zhang, G. Zhao, L. Li, P. Wang, L. Xie, B. Cheng, H. Li, Z. Lin, C. Xi, J. Ke, M. Yang, J. He, Z. Sun, Z. Wang, Z. Zhang, C. Zeng, *Proc Natl Acad Sci U S A* **2020**, *117*, 11337.
[6] Y. Zhang, Y. Sun, B. Yan, *Phys. Rev. B* **2018**, *97*, 041101.
[7] L. Wu, S. Patankar, T. Morimoto, N. L. Nair, E. Thewalt, A. Little, J. G. Analytis, J. E. Moore, J. Orenstein, *Nat. Phys.* **2017**, *13*, 350.
[8] N. Kumar, S. Najmaei, Q. Cui, F. Ceballos, P. M. Ajayan, J. Lou, H. Zhao, *Phys. Rev. B* **2013**, *87*, 161403.
[9] Y. Li, Y. Rao, K. F. Mak, Y. You, S. Wang, C. R. Dean, T. F. Heinz, *Nano Lett.* **2013**, *13*, 3329.
[10] X. Zhou, J. Cheng, Y. Zhou, T. Cao, H. Hong, Z. Liao, S. Wu, H. Peng, K. Liu, D. Yu, *J. Am. Chem. Soc.* **2015**, *137*, 7994.
[11] M. Zhao, Z. Ye, R. Suzuki, Y. Ye, H. Zhu, J. Xiao, Y. Wang, Y. Iwasa, X. Zhang, *Light Sci Appl* **2016**, *5*, 16131.
[12] Y. Song, S. Hu, M.-L. Lin, X. Gan, P.-H. Tan, J. Zhao, *ACS Photonics* **2018**, *5*, 3485.
[13] J. Zhou, J. Shi, Q. Zeng, Y. Chen, L. Niu, F. Liu, T. Yu, K. Suenaga, X. Liu, J. Lin, Z. Liu, *2D Mater.* **2018**, *5*, 025019.
[14] Q. Hao, H. Yi, H. Su, B. Wei, Z. Wang, Z. Lao, Y. Chai, Z. Wang, C. Jin, J. Dai, W. Zhang, *Nano Lett.* **2019**, *19*, 2634.
[15] Z. Sun, Y. Yi, T. Song, G. Clark, B. Huang, Y. Shan, S. Wu, D. Huang, C. Gao, Z. Chen, M. Mcguire, T. Cao, D. Xiao, W.-T. Liu, W. Yao, X. Xu, S. Wu, *Nature* **2019**, *572*, 497.
[16] J. Shi, P. Yu, F. Liu, P. He, R. Wang, L. Qin, J. Zhou, X. Li, J. Zhou, X. Sui, S. Zhang, Y. Zhang, Q. Zhang, T. C. Sum, X. Qiu, Z. Liu, X. Liu, *Adv. Mater.* **2017**, *29*, 1701486.
[17] J. Yu, X. Kuang, J. Li, J. Zhong, C. Zeng, L. Cao, Z. Liu, Z. Zeng, Z. Luo, T. He, A. Pan, Y. Liu, *Nat. Commun.* **2021**, *12*, 1083.
[18] M. Cheng, S. Wu, Z.-Z. Zhu, G.-Y. Guo, *Phys. Rev. B* **2019**, *100*, 035202.
[19] B. Jiang, Z. Hao, Y. Ji, Y. Hou, R. Yi, D. Mao, X. Gan, J. Zhao, *Light Sci Appl* **2020**, *9*, 63.
[20] K. Bredillet, J. Riporto, G. T. Forcherio, J. R. Dunklin, J.-P. Wolf, L. Bonacina, Y. Mugnier, R. Le Dantec, *Phys. Rev. B* **2020**, *102*, 235408.
[21] P. Cherin, P. Unger, *Acta Crystallogr.* **1967**, *23*, 670.
[22] A. S. Pine, G. Dresselhaus, *Phys. Rev. B* **1972**, *5*, 4087.
[23] W. Richter, *J. Phys. Chem. Solids* **1972**, *33*, 2123.

[24] X.-L. Liu, X. Zhang, M.-L. Lin, P.-H. Tan, *Chin. Phys. B* **2017**, *6*, 067802.
[25] C. Patel, *Phys. Rev. Lett.* **1965**, *15*, 1027.
[26] S. Panyakeow, Y. Tanigaki, J. Shirafuji, Y. Inuishi, *J. Appl. Phys.* **1972**, *43*, 4268.
[27] G. Sherman, P. Coleman, *IEEE J. Quantum Electron.* **1973**, *9*, 403.
[28] R. R. Silva, H. A. G. Mejia, S. J. L. Ribeiro, L. K. Shrestha, K. Ariga, O. N. Oliveira Jr., V. R. Camargo, L. J. Q. Maia, C. B. Araújo, *J. Braz. Chem. Soc.* **2017**, *28*, 58.
[29] X. Gan, J. Li, M. Xu, X. Wang, Z. Liu, J. Zhao, *Adv. Opt. Mater.* **2020**, *8*, 2001273.
[30] D. J. Clark, V. Senthilkumar, C. T. Le, D. L. Weerawarne, B. Shim, J. I. Jang, J. H. Shim, J. Cho, Y. Sim, M.-J. Seong, S. H. Rhim, A. J. Freeman, K.-H. Chung, Y. S. Kim, *Phys. Rev. B* **2014**, *90*, 121409.
[31] D. J. Clark, C. T. Le, V. Senthilkumar, F. Ullah, H.-Y. Cho, Y. Sim, M.-J. Seong, K.-H. Chung, Y. S. Kim, J. I. Jang, *Appl. Phys. Lett.* **2015**, *107*, 131113.
[32] Y. Song, R. Tian, J. Yang, R. Yin, J. Zhao, X. Gan, *Adv. Opt. Mater.* **2018**, *6*, 1701334.
[33] R. I. Woodward, R. T. Murray, C. F. Phelan, R. E. P. D. Oliveira, T. H. Runcorn, E. J. R. Kelleher, S. Li, E. C. D. Oliveira, G. J. M. Fechine, G. Eda, C. J. S. D. Matos, *2D Mater.* **2017**, *4*, 011006.
[34] G. Q. Ngo, E. Najafidehaghani, Z. Gan, S. Khazaee, M. P. Siems, A. George, E. P. Schartner, S. Nolte, H. Ebendorff-Heidepriem, T. Pertsch, A. Tuniz, M. A. Schmidt, U. Peschel, A. Turchanin, F. Eilenberger, *Nat. Photon.* **2022**, *16*, 769.
[35] B. Rabindra, P. Asish, A. S. K. Lal, M. Sruti, R. Varun, *Nanophoton* **2023**, *12*, 29.
[36] I. Abdelwahab, B. Tilmann, Y. Wu, D. Giovanni, I. Verzhbitskiy, M. Zhu, R. Bertè, F. Xuan, L. de, S. Menezes, G. Eda, T. C. Sum, S. Y. Quek, S. A. Maier, K. P. Loh, *Nat. Photon.* **2022**, *16*, 644.
[37] L. A. Agapito, N. Kioussis, W. A. Goddard, N. P. Ong, *Phys. Rev. Lett.* **2013**, *110*, 176401.
[38] I. Sodemann, L. Fu, *Phys. Rev. Lett.* **2015**, *115*, 216806.
[39] T. Morimoto, N. Nagaosa, *Sci. Adv.* **2016**, *2*, 1501524.
[40] G. Kresse, J. Furthmüller, *Phys. Rev. B* **1996**, *54*, 11169.
[41] G. Kresse, J. Furthmüller, *Comput. Mater. Sci.* **1996**, *6*, 15.
[42] P. E. Blöchl, *Phys. Rev. B* **1994**, *50*, 17953.
[43] G. Kresse, D. Joubert, *Phys. Rev. B* **1999**, *59*, 1758.
[44] J. Sun, A. Ruzsinszky, J. P. Perdew, *Phys. Rev. Lett.* **2015**, *115*, 036402.
[45] H. Peng, Z.-H. Yang, J. P. Perdew, J. Sun, *Phys. Rev. X* **2016**, *6*, 041005.
[46] A. A. Mostofi, J. R. Yates, Y.-S. Lee, I. Souza, D. Vanderbilt, N. Marzari, *Comput. Phys. Commun.* **2008**, *178*, 685.
[47] M. Taherinejad, K. F. Garrity, D. Vanderbilt, *Phys. Rev. B* **2014**, *89*, 115102.
[48] D. Xiao, M.-C. Chang, Q. Niu, *Rev. Mod. Phys.* **2010**, *82*, 1959.
[49] T. Fukui, Y. Hatsugai, H. Suzuki, *J. Phys. Soc. Jpn.* **2005**, *74*, 1674.
[50] C. Aversa, J. E. Sipe, *Phys. Rev. B* **1995**, *52*, 14636.